Nuclear Science and Techniques (2024) 35:220
https://doi.org/10.1007/s41365-024-01589-w

Imaging the initial condition of heavy-ion collisions and nuclear structure across the nuclide chart

Jiangyong Jia[1,2] · Giuliano Giacalone[3] · Benjamin Bally[4] · James Daniel Brandenburg[5] · Ulrich Heinz[5] · Shengli Huang[1] · Dean Lee[6] · Yen-Jie Lee[7] · Constantin Loizides[8] · Wei Li[8] · Matthew Luzum[9] · Govert Nijs[3] · Jacquelyn Noronha-Hostler[10] · Mateusz Ploskon[11] · Wilke van der Schee[3] · Bjoern Schenke[2] · Chun Shen[12,13] · Vittorio Somà[4] · Anthony Timmins[14] · Zhangbu Xu[2,15] · You Zhou[16]

Received: 16 October 2024 / Revised: 16 October 2024 / Accepted: 17 October 2024 / Published online: 11 December 2024

Abstract
High-energy nuclear collisions encompass three key stages: the structure of the colliding nuclei, informed by low-energy nuclear physics, the *initial condition*, leading to the formation of quark–gluon plasma (QGP), and the hydrodynamic expansion and hadronization of the QGP, leading to final-state hadron distributions that are observed experimentally. Recent advances in both experimental and theoretical methods have ushered in a precision era of heavy-ion collisions, enabling an increasingly accurate understanding of these stages. However, most approaches involve simultaneously determining both QGP properties and initial conditions from a single collision system, creating complexity due to the coupled contributions of these stages to the final-state observables. To avoid this, we propose leveraging established knowledge of low-energy nuclear structures and hydrodynamic observables to independently constrain the QGP's initial condition. By conducting comparative studies of collisions involving isobar-like nuclei—species with similar mass numbers but different ground-state geometries—we can disentangle the initial condition's impacts from the QGP properties. This approach not only refines our understanding of the initial stages of the collisions but also turns high-energy nuclear experiments into a precision tool for imaging nuclear structures, offering insights that complement traditional low-energy approaches. Opportunities for carrying out such comparative experiments at the Large Hadron Collider and other facilities could significantly advance both high-energy and low-energy nuclear physics. Additionally, this approach has implications for the future electron-ion collider. While the possibilities are extensive, we focus on selected proposals that could benefit both the high-energy and low-energy nuclear physics communities. Originally prepared as input for the long-range plan of U.S. nuclear physics, this white paper reflects the status as of September 2022, with a brief update on developments since then.

Keywords Nuclear structure · Heavy-ion collisions · Collective behavior · Quark–gluon plasma

1 Introduction: from nuclear structure to heavy-ion collisions

Collective behavior in many-body systems governed by the strong nuclear force emerges ubiquitously across energy scales and plays an instrumental role in our understanding of the phenomenology of such complex systems. In the zero temperature realm of atomic nuclei, strong collective correlations of nucleons lead to a range of fascinating structure properties, such as the emergence of rotational bands, which are naturally explained via notions of nuclear deformations and fluctuating intrinsic nuclear shapes [1]. At high temperatures, nucleons melt into fundamental constituents, quarks and gluons, to form the so-called quark–gluon plasma (QGP), whose collective description in terms of fluid dynamics has enabled us to explain a wealth of experimental data from high-energy nuclear collisions [2, 3].

Recently, collisions of ions of similar mass at high energy, such as in the BNL RHIC isobar run of ^{96}Ru+^{96}Ru and ^{96}Zr+^{96}Zr collisions, have led to the experimental demonstration of the direct impact of structural properties of nuclei on the collective flow of the produced QGP [4]. Enabling such a connection is the fact that high-energy collisions

Dedicated to Professor Wenqing Shen in honor of his 80th birthday.

Extended author information available on the last page of the article

probe, on an event-by-event basis, nucleon configurations from collapsed nuclear wave functions in the overlap region [5–7]. This is made possible by the ultra-short time duration for the interaction between the two ions at high energy. Sensitivity to individual realizations of nucleon configurations combined with the large number of particles produced in each high-energy collision (up to 30,000 particles in a Pb+Pb collision at CERN LHC energy [8]) enables a direct link between multi-particle correlations in the final state of the collisions and multi-nucleon correlations in the colliding nuclear states. The way high-energy collisions of nuclei access the nuclear structure is, therefore, akin to the techniques employed in the study of many-body correlations in highly controllable quantum systems, such as cold atom gases [9, 10], where the coordinates of individual constituents are measured via imaging techniques. High-energy collisions are the ideal tool for imaging the collective structure of atomic nuclei, as opposed to electron-nucleus scattering, where more local information about parton structure or short-range nucleon correlations is accessible.

A major research goal in high-energy nuclear physics is the characterization of the QGP in terms of medium properties, such as specific shear and bulk viscosities, η/s and ζ/s, or the jet quenching transport parameter, $\hat{q}$ [3]. The precision achievable in this characterization, e.g., in state-of-the-art Bayesian analyses [11–15], is impacted by our uncertain knowledge of the mechanism of energy deposition in the interaction of two nuclei. Assessing the role of the nuclear structure input will, therefore, reduce this uncertainty, permitting global analyses of data to infer cleaner information about the collision dynamics, and in turn the knowledge of the QGP initial condition [16]. Conversely, a major direction of research in nuclear structure theory focuses on the emergence of nuclear properties from fundamental theory [17]. Such *ab initio* approaches aim at describing strongly correlated nuclear systems from approximate (yet systematically improvable) solutions of the Schrödinger equation with nucleon–nucleon and three-nucleon interactions constructed in an effective theory of low-energy QCD. These efforts find a natural application in the phenomenology of multi-particle correlations in high-energy nuclear collisions. Once the response of the QGP initial condition to nuclear structure is established, one could use measurements in heavy-ion collisions to test the results of *ab initio* approaches in a way that is complementary to low-energy experiments. The systematic use of *ab initio* results as an input for the model building of nuclear collisions will then permit us to assess, in particular, the consistency of nuclear phenomena across energy scales.

Given the rapid progress in the development of *ab initio* theories of nuclear structure, and considering that the nuclear program at the CERN LHC in the next decade is largely to be defined, it is timely to identify the physics opportunities based on the synergy of these two areas from which the nuclear community as a whole could benefit.

2 Manifestation of nuclear structure in high-energy nuclear collisions

2.1 Methodology

Figure 1 illustrates the method for accessing the structure of ions colliding at relativistic energies. (A) Two nuclei are smashed in a high-energy collider (the large Lorentz contraction in the beam direction is not shown). (B) At the time of interaction, the nuclei are characterized by nontrivial geometries of nucleon configurations, including deformations and radial profiles. (C) The geometry of such configurations is reflected in the initial condition of

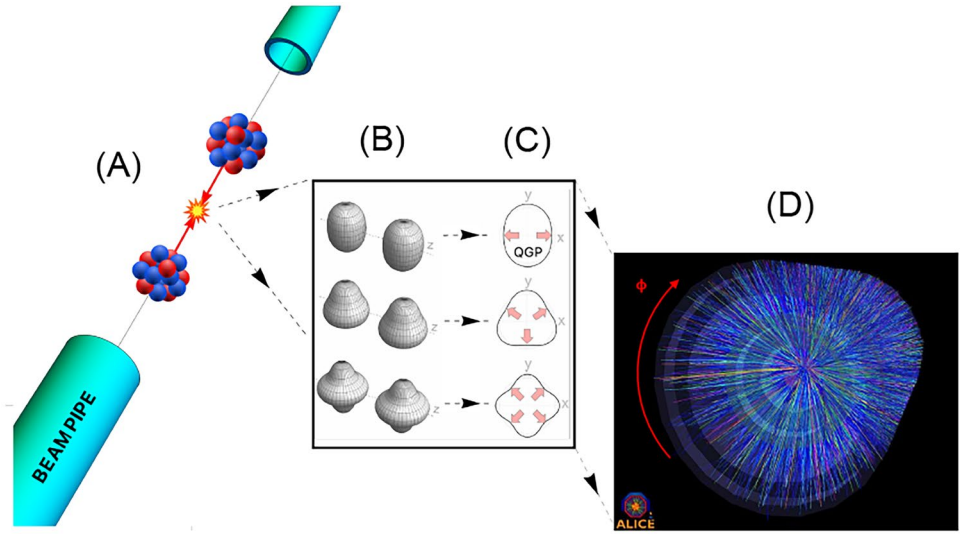

Fig. 1 (Color online) Schematic view of a relativistic heavy-ion collision, highlighting the role played by the collective properties of the colliding ions in shaping the geometry of the produced quark–gluon plasma (QGP). The Lorentz contraction of the two nuclei in the z-direction, by factor $\gamma \sim 100$ at the BNL RHIC or over 1000 at the CERN LHC, is not shown. See text for a detailed description

the created QGP. The subsequent hydrodynamic expansion of this system, driven by pressure-gradient forces, converts the spatial asymmetries in the initial shape into the momentum asymmetries of emitted particles in the transverse plane. (D) Experimentally, transverse momentum (p_T) asymmetries can be revealed via a Fourier expansion of the particle distributions in azimuthal angle:

$$\frac{d^2N}{dp_T d\phi} = \frac{dN}{2\pi dp_T}\left(1 + 2\sum_{n=1}^{\infty} v_n \cos n(\phi - \Phi_n)\right), \quad (1)$$

where the Fourier harmonics $V_n = v_n e^{in\Phi_n}$ are coefficients of anisotropic flow. The most significant harmonics are V_2, elliptic flow, reflecting the elliptical asymmetry of the geometry of the QGP, and V_3, reflecting the triangular asymmetry [18–20]. We note that the total particle multiplicity, $N_{ch} = \int dp_T dN/dp_T$, is proportional to the amount of energy deposited in a collision, which in turn is determined by the number of nucleons, N_{part}, participating in the interaction. The slope of the p_T spectra reflects the strength of the radial expansion, characterized by $\langle p_T \rangle = \frac{1}{N_{ch}} \int dp_T\, p_T dN/dp_T$, which is inversely related to the transverse size of the overlap region [21]. Due to these relations, inherent to the hydrodynamic description, information about the structure of the colliding ions can be inferred from the detected final-state particles.

The most direct way of observing the impact of the nuclear structure via this method is through comparing observables measured in collisions of species that are close in mass. Isobars, i.e., nuclides having the same mass number, are ideal candidates for such studies [16], as explicitly demonstrated by experimental data from ^{96}Zr+^{96}Zr and ^{96}Ru+^{96}Ru collisions, collected in 2018 at the BNL RHIC and released three years later [4]. Given two isobars, X and Y, and a given observable, $\mathcal{O}$, we ask the following question:

$$\boxed{\frac{\mathcal{O}_{X+X}}{\mathcal{O}_{Y+Y}} \overset{?}{=} 1} \quad (2)$$

Model studies have established that any visible departure from unity in the ratio must originate from differences in the structure of the isobars. In the measurements of the STAR collaboration, structure influences are ubiquitously found. Ratios of more than ten observables taken between ^{96}Zr+^{96}Zr and ^{96}Ru+^{96}Ru have been measured, all displaying distinct and centrality-dependent deviations from unity, as reported in Fig. 2 [22]. Such rich and versatile information can provide a new type of constraint on the structure of these isobars, as also predicted by early model investigations, which we discuss below.

2.2 Nuclear structure input

The hydrodynamic model of heavy-ion collisions successfully reproduces a vast set of experimental measurements at the BNL RHIC and the CERN LHC [23]. The input to hydrodynamic simulations is the event-by-event distribution of nucleons in the colliding ions. Motivated by low-energy nuclear physics, a Woods–Saxon profile with a nuclear surface expanded in spherical harmonics is routinely employed,

$$\rho(r,\theta,\phi) \propto \frac{1}{1 + e^{[r - R_0(1+\beta_2(\cos\gamma Y_2^0(\theta,\phi) + \sin\gamma Y_2^2(\theta,\phi)) + \beta_3 Y_3^0(\theta,\phi))]/a_0}}, \quad (3)$$

where R_0 is the half-density radius, a_0 is the surface diffuseness, β_2 is the magnitude of the quadrupole deformation, γ determines the relative length of the three axes of the ellipsoid, and β_3 is the (axial) octupole deformation parameter, where $\beta_3 \neq 0$ implies a breaking of parity symmetry in the intrinsic nuclear shape. Hydrodynamic simulations show that any changes in these parameters leave characteristic and detectable impacts on experimental observables such as those shown in Fig. 2 [24, 25].

Alternatively, hydrodynamic simulations can take pre-sampled nucleon configurations from *ab initio* calculations as input (See, e.g., Refs. [26–29] for such applications in ^{16}O collisions). Here, diffuseness and deformations emerge directly from many-nucleon correlations in the sampled wave functions. Given the expected rapid progress in the reach and quality of *ab initio* calculations over the next few years [17, 30], this alternative approach should become broadly adopted in the modeling of heavy-ion collisions in future. Full exploitation of such predictions of state-of-the-art nuclear theory will demonstrate further the scientific relevance of the connection between high-energy observations and low-energy theories.

2.3 Signatures of intrinsic nuclear shapes

A crucial observable in high-energy heavy-ion collisions is the rms flow coefficient, $v_n = \sqrt{\langle |V_n|^2 \rangle}$. Numerical and semi-analytical studies show that, for collisions at a given multiplicity (or centrality), v_n is enhanced by the presence of nuclear deformations in the colliding ions, following[16, 31–33],

$$v_n^2 \approx b_0 + b_1 \beta_n^2, \quad (4)$$

where b_0 and b_1 are positive coefficients that depend on centrality. The enhancement predicted by Eq. (4) would show up, in particular, when comparing collisions of deformed nuclei to collisions of spherical nuclei. A powerful way to do so is to compare deformed ion collisions with collisions

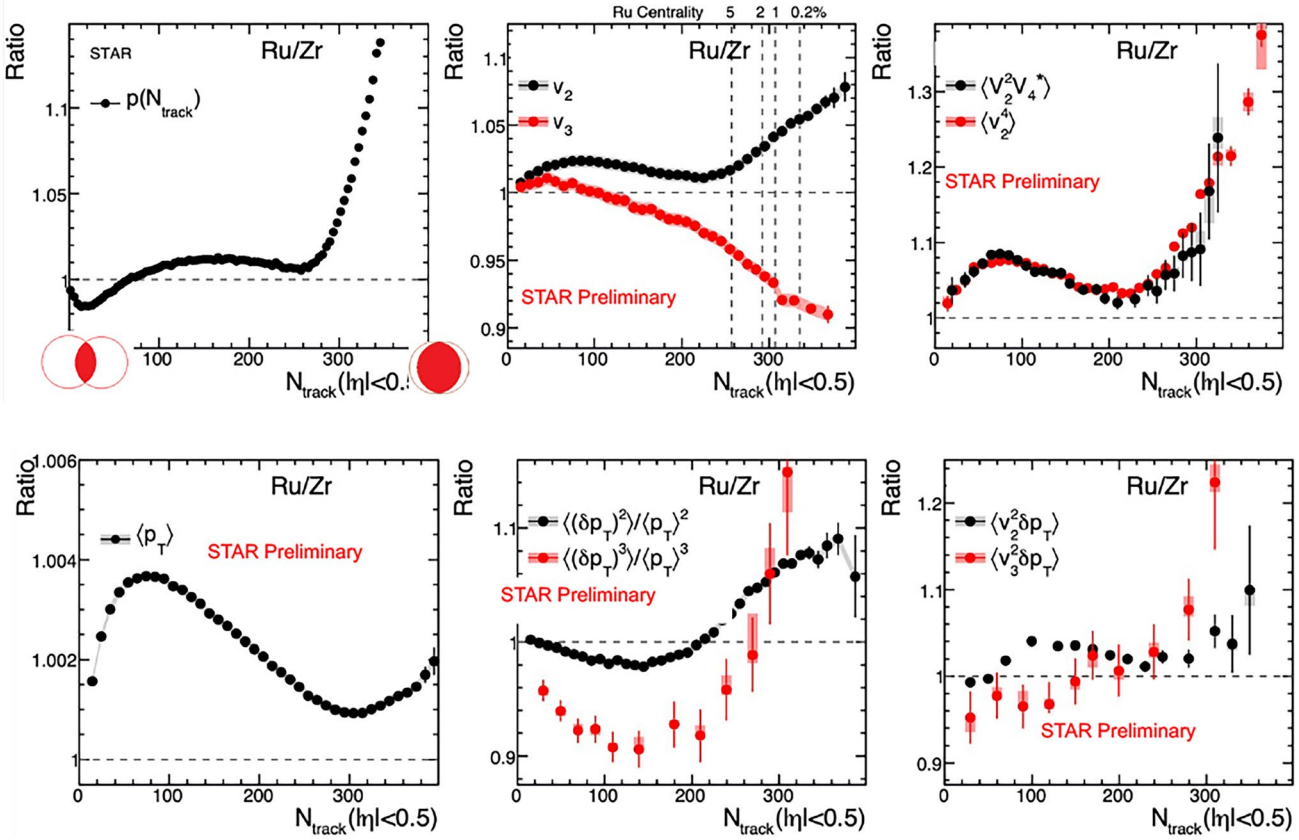

Fig. 2 (Color online) Ratios of observables taken between ^{96}Ru+^{96}Ru and ^{96}Zr+^{96}Zr collisions as a function of $N_{\rm ch}$, as measured by the STAR Collaboration (Preliminary results). A total of ten ratios are shown

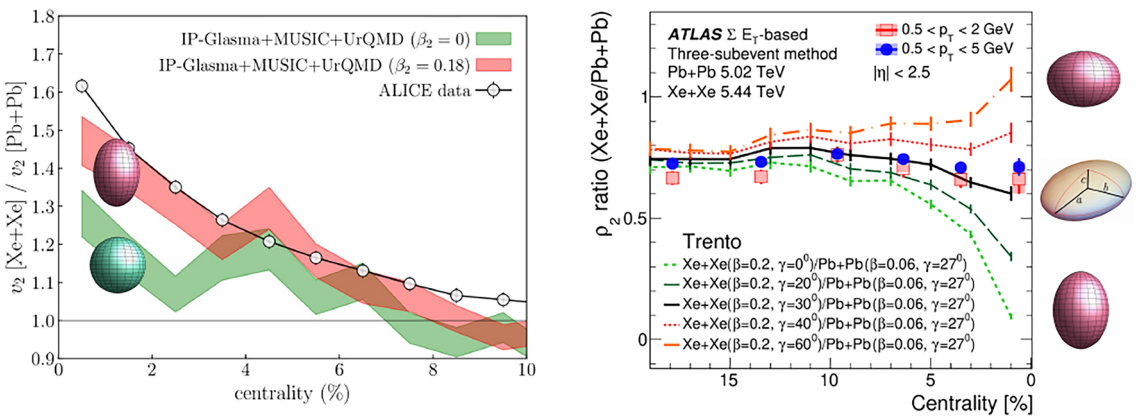

Fig. 3 (Color online) Modification of multi-particle correlation observables in Xe+Xe collisions compared to the baseline with spherical nuclei provided by Pb+Pb collisions. Left: elliptic flow, v_2 [35]. Right: correlation between elliptic flow and the average transverse momentum, ρ_2 [45]

of nearly spherical ^{208}Pb ions. The left panel of Fig. 3 reveals an enhanced v_2 in ^{129}Xe+^{129}Xe collisions compared to ^{208}Pb+^{208}Pb collisions [34], as observed by the ALICE collaboration [35]. A state-of-the-art calculation [36] confirms the origin of this effect due to the large β_2 of ^{129}Xe.

Concerning the triaxiality, γ in Eq. (1), revealing its presence requires the use of three-particle correlations. The most sensitive observable is the correlation of the shape of the QGP with its size [37], measurable experimentally via a correlation between v_n^2 and the fluctuation

of transverse momentum, $\delta p_T = p_T - \langle p_T \rangle$, at a given multiplicity. This quantity is conveniently formulated as a Pearson coefficient [38], $\rho_n = \frac{\langle v_n^2 \delta p_T \rangle}{\sqrt{\left(\langle v_n^4 \rangle - \langle v_n^2 \rangle^2\right)} \sqrt{\langle \delta p_T \delta p_T \rangle}}$. For quadrupole deformation, theoretical work shows the following leading-order dependence [39]

$$\rho_2 \approx b_0' - b_1' \beta_2^3 \cos(3\gamma), \tag{5}$$

where b_0' and b_1' are positive coefficients. In the presence of large β_2, moving from oblate ($\gamma = 60°$) to prolate ($\gamma = 0$) shapes decreases ρ_2 in a substantial way. A recent measurement at RHIC shows precisely $\rho_2 < 0$ in central U+U collisions [40], which is explained naturally by the large prolate deformation of ^{238}U [41], $\beta_2 \sim 0.28$, $\gamma = 0$. The nucleus ^{129}Xe is particularly interesting for such a study, as its shape is considerably deformed and also triaxial, $\beta_2 = 0.2$ and $\gamma \approx 30°$ [42–44]. In the right panel of Fig. 3, model calculations assuming oblate, triaxial, and prolate ^{129}Xe shape show a strong modification of ρ_2 in ^{129}Xe+^{129}Xe collisions with respect to the ^{208}Pb+^{208}Pb collisions [43]. Measurements from the ATLAS collaboration indeed confirm the triaxial scenario [45]. One important point is that the combined use of v_2^2 and ρ_2 can simultaneously constrain β_2 and γ.

In the octupole sector, much less is known from low-energy physics [46]. Direct evidence of octupole deformation in excitation bands of atomic nuclei is scarce, because octupole deformation rarely manifests as a mean-field effect (*static* deformations) [47, 48], as in a simple rotor model. However, *dynamical* octupole correlations at the beyond-mean-field level are present in essentially all nuclei [49] and should leave their fingerprint in the nucleon configurations from *ab initio* calculations. High-energy nuclear collisions, probing configurations of nucleons on an event-by-event basis, give access to all such non-static deformations in the ground states in the same way as the static ones.

One of the breakthrough outcomes of the isobar collision campaign at RHIC is reported in Fig. 4, also shown in the mid-bottom panel of Fig. 2. The ratio of v_n taken between Ru+Ru and Zr+Zr collisions shows significant departures from unity. The data imply that ^{96}Ru has a larger β_2 than ^{96}Zr, as expected from low-energy experiments. A similar departure for $n = 3$, showing an enhanced v_3 in Zr+Zr collisions, can only be ascribed to ^{96}Zr having a sizable β_3 [50], which is not predicted by mean-field energy density functional calculations [48, 51]. The results of the STAR collaboration demonstrate that heavy-ion collisions offer a clean access route to multi-nucleon correlations that are both difficult to quantify from traditional low-energy experiments and hard to predict from phenomenological models.

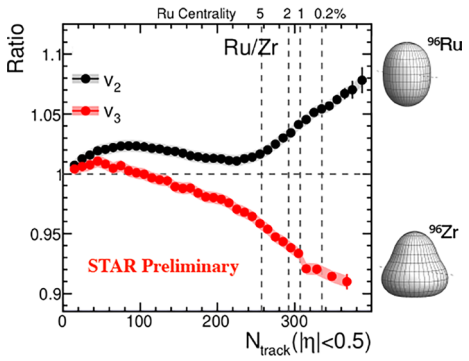

Fig. 4 (Color online) Preliminary ratios of flow coefficients, v_n, taken between Ru+Ru and Zr+Zr collisions. The suppression of the v_3 ratio at large multiplicity is due to an enhancement of v_3 in Zr+Zr collisions

2.4 Radial profiles and relation to neutron distributions

The nuclear radial profile, determined by the R_0 and a_0 parameters in Eq. (2), influences the area and the density of the overlap region. In general, a smaller a_0 or R_0 for a fixed mass number leads to a sharper edge in the overlap geometry, leading to a more compact QGP, larger pressure gradients, and hence larger $\langle p_T \rangle$ and v_n. The impact is more significant in off-central collisions where the overlap region is smaller, and sensitivity to a variation in R_0 and a_0 is larger. Indeed, model studies show that the probability distributions of $N_{\rm part}$, and hence the distribution of $N_{\rm ch}$, $p(N_{\rm ch})$, as well as $\langle p_T \rangle$ and v_2, are largely impacted by variations in a_0 and R_0 [24, 52, 53].

Due to model-dependent systematics, constraining the radial nuclear profile in a single collision system is difficult. Such limitation is largely overcome by comparing experimental observables between systems close in size, such as isobars. Assuming the differences of radial parameters are small, deviation of isobar ratios from unity can be approximated by (taking ^{96}Ru and ^{96}Zr as an example)

$$\frac{\mathcal{O}_{\rm Ru}}{\mathcal{O}_{\rm Zr}} \approx 1 + c_0(R_{0,\rm Ru} - R_{0,\rm Zr}) + c_1(a_{0,\rm Ru} - a_{0,\rm Zr}), \ \mathcal{O} \equiv p(N_{\rm ch}), v_2, \text{ or } \langle p_T \rangle, \tag{6}$$

where the coefficients c_0 and c_1 depend only on the mass number at a given centrality or multiplicity and are insensitive to the final state effects [54]. These simple equations describe well the isobar ratios, as verified in recent transport model simulations [24].

Energy density functional calculations suggest that ^{96}Zr has a larger diffuseness but a smaller radius than ^{96}Ru, i.e., $\Delta a_0 \equiv a_{0,\rm Ru} - a_{0,\rm Zr} < 0$ and $\Delta R_0 \equiv R_{0,\rm Ru} - R_{0,\rm Zr} > 0$ [56, 57]. As shown in Fig. 5, a transport calculation implementing such differences can quantitatively describe the

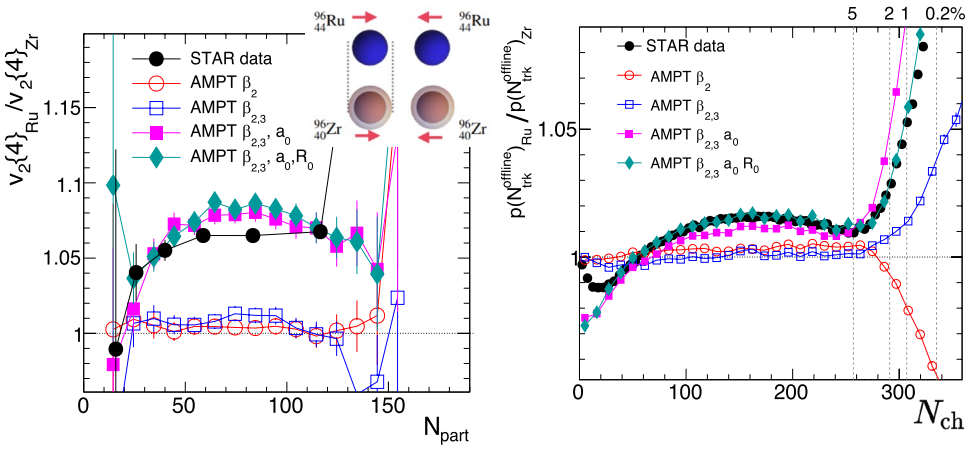

Fig. 5 (Color online) Ratios of observables taken between Ru+Ru and Zr+Zr collisions. The inset in the left panel shows how the neutron excess of ^{96}Zr compared to ^{96}Ru yields a more diffuse nuclear surface, i.e., a larger a_0 and a slightly smaller R_0 in Eq. (1). Left: the impact of the larger a_0 of ^{96}Zr manifests predominantly in the fourth-order cumulant of v_2, $v_2\{4\}$, which originates from the intrinsic ellipticity of the QGP due to the finite collision impact parameter. Right: both a_0 and R_0 differences contribute to a broad hump in the ratio of $p(N_{\rm ch})$. Calculations are obtained within the A Multi-Phase Transport (AMPT) model [55]

measured ratios of $v_2\{4\}$ (the fourth-order cumulant of elliptic flow fluctuations) and of the distribution of charged particle number, $p(N_{\rm ch})$. The cumulant $v_2\{4\}$ measures the flow originating from the intrinsic ellipticity acquired by the QGP due to the finite impact parameter of the collisions [58]. Figure 5 shows that such intrinsic ellipticity is impacted only by Δa_0 [59], but is insensitive to ΔR_0 and nuclear deformations. On the other hand, $p(N_{\rm ch})$-ratio is sensitive to both Δa_0 and ΔR_0 [56, 57]. A dedicated study finds that the ratio of $p_{\rm T}$ is also sensitive to both Δa_0 and ΔR_0 [53]. Therefore, the measurement of isobar ratios provides several independent determinations on the differences ΔR_0 and Δa_0, which can be confronted against the predictions of low-energy nuclear structure models.

The knowledge of nucleon distribution, in combination with the well-known proton distribution parameters $a_{\rm p}$ and $R_{0\rm p}$ from low-energy experiments, allows one to probe the difference between the rms radius of neutrons and protons in heavy nuclei, $\Delta r_{\rm np} = R_{\rm n} - R_{\rm p}$, known as the neutron skin. The value of $\Delta r_{\rm np}$ is directly related to the slope of the symmetry energy, dubbed L, appearing in the equation of state (EOS) of nuclear matter [60]. Determinations of L are intensively pursued at low energy because this parameter plays a crucial role in the stability properties of neutron stars [61, 62]. Isobar ratios in high-energy collisions are expected to probe only the difference in the neutron skin, $\Delta(\Delta r_{\rm np}) = \Delta r_{\rm np,Ru} - \Delta r_{\rm np,Zr}$. Assuming Woods–Saxon distributions for protons and nucleons, $\Delta r_{\rm np}$ receives a contribution from both half-radius and surface diffuseness [24]: $\Delta(\Delta r_{\rm np}) \propto (R_0 \Delta R_0 - R_{0\rm p}\Delta R_{0\rm p}) + 7/3\pi^2(a\Delta a - a_{\rm p}\Delta a_{\rm p})$. Therefore, collisions of isobars or, in general, of species of similar mass numbers allow one to access detailed information about radial profiles and neutron skins of nuclei systematically.

3 Science cases at the intersection of nuclear structure and hot QCD

A window to perform collisions with new ions will be opened in future at the CERN LHC beyond Run3 (2025) and possibly before the shutdown of the BNL RHIC upon successful completion of the sPHENIX program. About 250 stable isotopes in the nuclear chart could be used systematically for such a purpose. About 140 are found in isobar pairs or triplets, as in Table 1. Our idea is to select nuclear species that would permit us to (1) probe features of high-energy collisions, in particular their initial condition, by exploiting well-known structural properties, (2) extract structure information of the colliding ions that would complement the effort of low-energy experiments, (3) reveal features of colliding ions that are difficult to access in conventional nuclear structure experiments, but have a significant impact on low-energy models. Continued effort is required to identify species that can maximize the scientific impact for both the hot QCD and the nuclear structure communities. For the moment, we have identified four cases that may lead to discoveries via high-energy experiments. They involve nuclides belonging to the mass regions $A \sim 20$, $A \sim 40$, $A \sim 150$, $A \sim 200$. More cases are expected to emerge upon further discussion and model studies (see Sect. 4 for a brief progress update since 2022).

Table 1 Pairs and triplets of stable isobars (half-life > 10^8 y)

A	isobars	*A*	isobars	*A*	isobars	*A*	isobars	*A*	isobars	*A*	isobars
36	Ar, S	80	Se, Kr	106	Pd, Cd	124	Sn, Te, Xe	**148**	**Nd, Sm**	174	Yb, Hf
40	Ca, Ar	84	Kr, Sr, Mo	108	Pd, Cd	126	Te, Xe	150	Nd, Sm	176	Yb, Lu, Hf
46	Ca, Ti	86	Kr, Sr	110	Pd, Cd	128	Te, Xe	152	Sm, Gd	180	Hf, W
48	Ca, Ti	87	Rb, Sr	112	Cd, Sn	130	Te, Xe, Ba	154	Sm, Gd	184	W, Os
50	Ti, V, Cr	92	Zr, Nb, Mo	113	Cd, In	132	Xe, Ba	156	Gd,Dy	186	W, Os
54	Cr, Fe	94	Zr, Mo	114	Cd, Sn	134	Xe, Ba	158	Gd,Dy	187	Re, Os
64	Ni, Zn	96	Zr, Mo, Ru	115	In, Sn	136	Xe, Ba, Ce	160	Gd,Dy	190	Os, Pt
70	Zn, Ge	98	Mo, Ru	116	Cd, Sn	138	Ba, La, Ce	162	Dy,Er	192	Os, Pt
74	Ge, Se	100	Mo, Ru	120	Sn, Te	142	Ce, Nd	164	Dy,Er	196	Pt, Hg
76	Ge, Se	102	Ru, Pd	122	Sn, Te	144	Nd, Sm	168	Er,Yb	198	Pt, Hg
78	Se, Kr	104	Ru, Pd	123	Sb, Te	**146**	**Nd, Sm**	170	Er,Yb	204	Hg, Pb

141 nuclides are listed. The region marked in italics contains large strongly deformed nuclei ($\beta_2 > 0.2$). The region marked in bold corresponds to nuclides which may present an octupole deformation in their ground state [48].

3.1 Stress-testing small system collectivity with ^{20}Ne

The neon-20 nucleus presents the most extreme ground state of all stable nuclides with $A > 10$. It is a strongly deformed object made of five α-clusters in a reflection-asymmetric α+^{16}O molecular configuration [63–65]. In terms of the common quadrupole deformation coefficient, the ground state has $\beta_2 \approx 0.7$, the highest of all stable ground states. The deformation of this nucleus is so large that its impacts can easily survive the large event-by-event fluctuations associated with sampling a small number of nucleons ($\propto 1/\sqrt{A}$). The extreme geometry of ^{20}Ne enables us to perform nontrivial tests of the initial-state modeling and the hydrodynamic response in small systems. In particular, one can compare collisions of highly-deformed N_{20} nuclei with collisions of nearly spherical O_{16} nuclei, the latter collisions have already been recorded at RHIC and are planned for 2025 at the LHC. The ratios of observables between the two systems will be largely independent of final state transport properties and hence directly access the variation in the initial condition caused by nuclear structure differences. Having data from ^{20}Ne+^{20}Ne collisions will maximize the scientific output of the ^{16}O+^{16}O run (and vice versa). On the side of nuclear structure theory, *ab initio* approaches have recently been pushed to describe light systems up to $A \sim 40$ [17], including ^{20}Ne [66]. Strong deformations in these approaches emerge from genuine n-body (up to A-body) correlations in the wavefunction generated by inter-nucleon interactions linked to QCD via an effective field theory. Precise measurement of multi-particle correlations in ^{20}Ne+^{20}Ne collisions will provide novel tests of the effectiveness of such *ab initio* calculations in capturing collective effects in strongly correlated nuclei.

As a bonus, while collecting ^{20}Ne+^{20}Ne collisions in collider mode at 7 TeV, one can have the same collisions in fixed-target mode at around 0.07 TeV by injecting a ^{20}Ne gas in the SMOG system of the LHCb experiment [67]. This would enable a study of the $\sqrt{s_{\rm NN}}$ dependence of the initial condition, longitudinal dynamics and geometry of small systems. Another, potentially superior way of imaging the structure of light nuclei is to collide them with heavy spherical nuclei, such as in ^{16}O+^{208}Pb or ^{20}Ne+^{208}Pb [68, 69]. The shape of overlap region at small impact parameter directly captures the nucleon distribution in light nuclei. Ratios of observables between ^{16}O+^{208}Pb and ^{20}Ne+^{208}Pb collisions will reveal the shape differences between ^{16}O and ^{20}Ne. The main advantage over symmetric ^{16}O+^{16}O and ^{20}Ne+^{20}Ne collisions is that asymmetric "isobar"+Pb collisions produce much more particles and will have a better centrality resolution [67]. This idea may be extended to even smaller systems such as ^{8}Be+^{208}Pb and ^{12}C+^{208}Pb [68, 69]. Collisions of asymmetric systems are feasible at the BNL RHIC (as demonstrated by the p+Au, d+Au and ^{3}He+Au runs [70]) but not at the CERN LHC in collider mode. However, asymmetric collisions can be performed in fixed-target mode by injecting oxygen-16 and neon-20 ions in the SMOG system of the LHCb detector [71] (a small sample of Ne+Pb data was collected in 2013).

3.2 Shape evolution along the Samarium isotopic chain

Certain isotopic chains in the nuclear chart exhibit strong variations in nuclear shapes. While this occurs mainly away

from the stability line, the chain of eight stable samarium isotopes (Sm $Z = 62$) features a transition from nearly spherical to strongly deformed nuclei with increasing neutron number, e.g., from ^{144}Sm with $\beta_2 \approx 0.09$, to ^{154}Sm with $\beta_2 \approx 0.34$, with a change in mass number of only about 7%. Since the hydrodynamic response is expected to be essentially constant over the isotopic chain, these systems offer a strong lever-arm to probe in detail how the initial condition of QGP responds to varying nuclear shapes, e.g., by predicting the coefficients b_0 and b_1 in Eq. (4) using two Sm isotopes and then make predictions of β_2 for other isotopes [33]. The β_2 differences among isotopes can be extracted from ratios of flow observables, as done for the BNL RHIC isobar run. The extracted differences from heavy-ion collisions can be compared with nuclear structure knowledge, to study whether shapes evolve similarly when adding neutrons one-by-one in low-energy experiments and high-energy collisions. We stress that these nuclei have been subject of much investigation at low energy, where their properties are nicely consistent across experiments and theoretical frameworks.

It is worth noting, then, that scanning the Sm isotopic chain in high-energy collisions would provide new experimental insight onto the octupole deformations of such nuclei. As demonstrated by the isobar ratios, nontrivial results are expected. Clear observation of octupole and potentially hexadecapole deformations for such nuclei would showcase the discovery potential of high-energy nuclear collisions as a tool to observe the manifestations of many-body correlations of nucleons in the ground state of nuclei, in a way that is fully complementary to low-energy structure experiments. In turn, this will provide new experimental constraints to test future *ab initio* calculations of such large and deformed systems.

3.3 The neutron skin of ^{48}Ca and ^{208}Pb in high-energy collisions

In low-energy experiments, the neutron skins of ^{48}Ca and ^{208}Pb, two doubly magic nuclei with a considerable neutron excess, have been the subject of much work. Dedicated experiments at Jefferson Lab have been devoted to measuring the neutron skin of these species [72, 73]. The measured value for ^{208}Pb is $\Delta r_{\rm np} = 0.28 \pm 0.07$ fm, which is systematically larger than predictions from energy density functional theories. The properties of neutron stars (e.g., the tidal deformability) resulting from such a constraint on the EOS turn out to be slightly at variance with those inferred from pulsar and gravitational wave observations, which has sparked intense debate in the community [74, 75]. The neutron skin of ^{48}Ca is instead more in line with the theoretical expectations. We aim to provide new constraints on the neutron skins of ^{48}Ca and ^{208}Pb by utilizing high-energy collisions.

Providing a robust estimate of the neutron skin of ^{48}Ca in high-energy nuclear collisions is rather straightforward. The isotopic chain of calcium has two doubly magic nuclei, ^{48}Ca and ^{40}Ca. The latter has the same number of protons and neutrons, and its neutron skin is much smaller than that of ^{48}Ca. However, experiments reveal that ^{48}Ca and ^{40}Ca have essentially the same charge radius with a difference less than 0.001 fm [76, 77], such that neutrons alone determine the differences in size between these two isotopes. As discussed in Sect. 2.4, heavy-ion collisions allow one to experimentally access differences in the neutron skins between nuclei of similar mass. Therefore, if $\Delta r_{\rm np}(^{48}{\rm Ca}) \gg \Delta r_{\rm np}(^{40}{\rm Ca}) \approx 0$, collisions of such nuclei could isolate

$$\Delta r_{\rm np}(^{48}{\rm Ca}) - \Delta r_{\rm np}(^{40}{\rm Ca}) \simeq \Delta r_{\rm np}(^{48}{\rm Ca}). \tag{7}$$

We estimate that this quantity can be accessed with an uncertainty of about 0.02 fm. Any significant deviations from the expectations of low-energy theories or experiments should be ascribed to the modification of the partonic structure of nucleons in nuclear environment at high energy.

Following this idea, the constraints on neutron skin of ^{208}Pb could be obtained by comparing data from ^{208}Pb+^{208}Pb with data from ^{197}Au+^{197}Au, as the two species are nearly isobars. Therefore, having such collisions at the same beam energy would allow us to determine the difference $\Delta r_{\rm np.Pb} - \Delta r_{\rm np.Au}$ from observables such as $v_2\{4\}$. This information could be combined with an additional estimate of the neutron skin from a method recently developed by the STAR collaboration [78], also at high energy. This method employs the production of ρ^0 mesons in photo-nuclear processes in ultra-peripheral collisions using the newly developed spin interference enabled nuclear tomography. The cross section for ρ^0 production in dipole-nucleus scattering contains a coherent component determined by the gluon distribution of the target nucleus. Fits of the coherent diffractive $|t|$ distribution within a Woods–Saxon geometry model in ^{197}Au+^{197}Au collisions lead to $\Delta_{\rm np}(^{197}{\rm Au}) = 0.17 \pm 0.03({\rm stat.}) \pm 0.08({\rm sys})$ fm. This method could be readily applied to other species such as ^{208}Pb via ^{208}Pb+^{208}Pb collisions. It would measure the neutron skin of ^{208}Pb with an uncertainty that is similar to or even better than that obtained by the PREX-II experiment. We emphasize that the systematic errors are largely correlated in this technique. The experiment should be able to demonstrate whether the extracted neutron skin difference between ^{208}Pb and ^{197}Au is compatible with low energy models and measurements (including PREX-II for Pb [72]). We note that a short Pb+Pb collision run at RHIC would be sufficient for this purpose. This is a cost-effective experiment with significant impacts on the nuclear physics community as a whole.

Furthermore, it is worth noting that at the energy reached at the LHC, electro-weak (EW) bosons are abundantly

produced in nucleus–nucleus collisions via $u\bar{d} \to W^+$, $d\bar{u} \to W^-$, and $q\bar{q} \to Z$ processes. These real EW bosons probe the weak charge distributions in the heavy-ion initial state, i.e., the sum of weak charge distributions from the two colliding nuclei in the overlap region. Therefore, isobar ratios of W and Z boson yields as a function of centrality may provide direct access to the radial distribution of valence and sea quarks, offering an access route to charge radius, mass radius and thus the neutron skin, and compare with that extracted from the PREX-II analysis of the neutral weak form factor of ^{208}Pb [79] associated with virtual Z boson. Based on 1 nb^{-1} 5.02 TeV Pb+Pb data (from one month of typical heavy-ion running), we expect each LHC experiment to deliver about 600k W bosons and 20k Z bosons reconstructed in the lepton decay channel [80, 81]. If isobar or isobar-like collisions such as ^{40}Ca+^{40}Ca vs. ^{48}Ca+^{48}Ca, or ^{208}Pb+^{208}Pb vs. ^{197}Au+^{197}Au become available at LHC, it will be possible to compute ratios of W and Z boson yields as a function of centrality with a statistical uncertainty of order 1% ($\sqrt{1/10000}$). This could be achieved in particular at the high-luminosity LHC, in Run5 or beyond (> 2035) [82, 83].

3.4 Initial conditions of heavy-ion collisions

The success of the hydrodynamic framework of heavy-ion collisions enables us today to perform quantitative extractions of the transport properties of the QGP via multi-system Bayesian analyses [11–15]. A major limitation of such extractions is the lack of precise control on the initial condition of the QGP prior to the hydrodynamic expansion. Insights about the energy deposition from two collided nuclei come from the color glass condensate (CGC) effective theory of high-energy QCD [84]. There, for a given boosted nuclear profile described by the *thickness* function $T = \int \rho(x, y, z)\mathrm{d}z$, the average energy density deposited in the transverse plane in the collision of, say, nuclei A and B, at the instant immediately after the collision occurs is of the form [85]

$$\langle T^{00} \rangle \, [\mathrm{GeV/fm^3}] \propto T_A T_B. \tag{8}$$

Bayesian analyses of heavy-ion data, while constraining transport properties of the QGP, attempt as well to constrain the initial conditions of the collisions. The prediction of the CGC in Eq. (8) can be tested via a generic parameterized Ansatz for the energy density, such as the T$_\mathrm{R}$ENTo Ansatz for the energy density per unit rapidity, $\mathrm{d}E/\mathrm{d}y$ [GeV/fm^2], namely $\mathrm{d}E/\mathrm{d}y \propto (\hat{T}_A^p + \hat{T}_B^p)^{1/p}$ [86], or its generalized version, $\mathrm{d}E/\mathrm{d}y \propto (\hat{T}_A^p + \hat{T}_B^p)^{q/p}$ [23, 87], where $\hat{T}$ represents the thickness function constructed solely from the participant nucleons within the colliding ions. The values of p and q and other model parameters such as nucleon width w and inter-nucleon minimum distance d_{min}can then be inferred from the analysis of high-energy collision data.

However, information about the content of the colliding nuclei, which cannot be predicted based on the CGC alone, yields a significant uncertainty in our understanding of the energy deposition itself and, in turn, of the QGP transport parameters resulting from fits to data. One example is provided by v_3 in Zr+Zr collisions. If one attempted to reproduce the measured v_3 in hydrodynamic calculations without implementing any β_3 parameter for such a nucleus, one would correct a 10% enhancement of such an observable in central collisions by biasing the extraction of other QGP transport or initial-state properties dramatically. It is the knowledge of the presence of a large octupole deformation from the isobar ratio $v_{3,\mathrm{Zr}}/v_{3,\mathrm{Ru}}$, that enable us to avoid biasing the extracted QGP features. Bayesian approaches have not yet systematically explored the impact of nuclear shape and radial distributions. Nuclear structure knowledge should be used systematically as a new lever arm to probe the initial condition of collisions of species that are close in mass and thus obtain better determinations of the QGP transport coefficients.

As discussed in Sect. 2.1, the deviation of isobar ratios from unity probes directly the structural differences between the two species, and the way the initial condition is shaped by two colliding ions. Numerical work shows that the ratios of many observables can be expressed in terms of the differences of Woods–Saxon parameters as a generalization of Eq. (6) [24],

$$\begin{aligned}\frac{\mathcal{O}_{\mathrm{Ru}}}{\mathcal{O}_{\mathrm{Zr}}} \approx 1 &+ c_0(R_{0,\mathrm{Ru}} - R_{0,\mathrm{Zr}}) \\ &+ c_1(a_{0,\mathrm{Ru}} - a_{0,\mathrm{Zr}}) + c_2(\beta^2_{2,\mathrm{Ru}} - \beta^2_{2,\mathrm{Zr}}) + c_3(\beta^2_{3,\mathrm{Ru}} - \beta^2_{3,\mathrm{Zr}}),\end{aligned} \tag{9}$$

with $\mathcal{O} \equiv p(N_{\mathrm{ch}}), v_2$, or $\langle p_{\mathrm{T}} \rangle$. Crucially, these ratios are insensitive to variations of QGP transport properties [54]. Therefore, the left-hand side of Eq. (9) captures the variations of initial conditions in the isobar systems, which are related to the structure parameters on the right-hand side. The coefficients c_n reflect how the initial condition changes when the nuclear structure is varied between the isobars. Via isobar collisions, thus, one can conveniently separate the role played by low-energy nuclear structure input (R_0, a_0, β_2^2, β_3^2) and role played by constraints from the knowledge of high-energy heavy-ion collisions (c_i coefficients) for observables (isobar ratios) that depend solely on the initial condition of the QGP, as illustrated in Fig. 6.

Collisions from pp, p+A and A+A have been collected at the BNL RHIC and the CERN LHC. For A+A collisions, we have ^{238}U+^{238}U and ^{197}Au+^{197}Au collisions at the BNL RHIC, and ^{129}Xe+^{129}Xe and ^{208}Pb+^{208}Pb collisions at the CERN LHC. However, none of these pairs

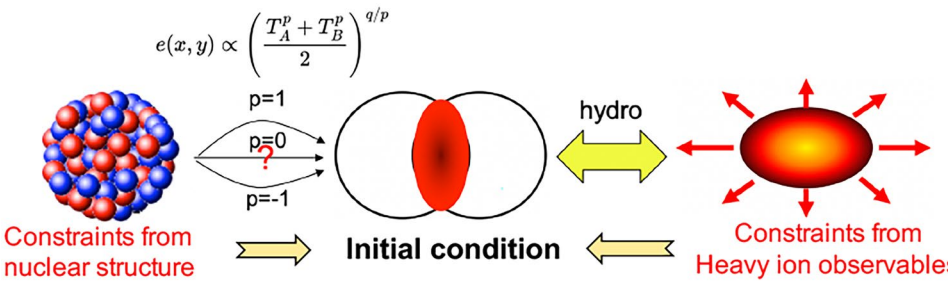

Fig. 6 (Color online) Impact of isobar-like collisions on the goal of the heavy-ion program. Better control on the initial condition can be achieved by exploiting the constraints from both the ratios of final-state observables and the nuclear structure knowledge

are close enough in their mass number [1], which means that the final-state effects do not completely cancel in the ratios [34]. The model dependencies of these residual effects are then significant enough to preclude a precise extraction of the initial condition. Colliding isobars, or in general species close in mass, such as ^{197}Au and ^{208}Pb, represents an ideal way to constrain the initial condition across the nuclide chart.

Concerning the possibility of having Pb+Pb reference data at the BNL RHIC, there are two arguments in the context of hot QCD studies to motivate such an effort, in addition to the neutron skin case pointed out in Sect. 2.3. (1) Being doubly magic, ^{208}Pb is essentially spherical. In contrast, ^{197}Au has a modest oblate deformation. For the high-precision studies of Au+Au collisions expected from the upcoming sPHENIX program, it would be important, then, to have Pb+Pb collisions as a tool to calibrate the initial condition of Au+Au collisions and ensure that the expectations of the low-energy nuclear theory are compatible with the observations at high energy. (2) Having Pb+Pb systems would also provide a bridge to compare the outcome of Pb+Pb collisions at the BNL RHIC to that of Pb+Pb collisions at the CERN LHC, to study the beam energy dependence of observables. For both these goals, a short Pb+Pb run at the BNL RHIC would be sufficient.

Last but not least, isobar or isobar-like collisions may serve as novel probes of the hard sector, via the analysis of observables such as the production of leading hadron, jets, photons, and heavy flavors. It has already been shown that collective flow of D-mesons is sensitive to the deformation of the nucleus [88]. Additionally, by constructing ratios of selected observables at a given centrality, or multiplicity, final state effects such as jet quenching are expected to cancel. Deviations from unity in the constructed ratios will provide access to flavor-dependent Nuclear Parton Distribution Function (nPDF), tailored for each underlying hard-scattering process. Interestingly, the precision determination of the impact parameter from bulk particles in coincidence with hard processes means that we can use isobar ratios to detect differences in the transverse spatial distribution of partons at given longitudinal momentum fraction between the two isobars.

One such example is already discussed in Sect. 3.3 in the context of W and Z bosons for neutron skin measurements. For some of the hard probes, such as high-p_{T} charged hadrons or inclusive jets, production will be so abundant that even a short run would permit one to determine the isobar ratio with a statistical precision of 1% or better as a function of centrality, with large cancelation of the systematical uncertainties. One could also study how the isobar ratio evolves with rapidity to detect potential modifications to the nuclear structure inputs due to nPDF or gluon saturation. Isobar ratios of more differential measurements, such as dijet or photon-jet measurements, could probe in more detail the correlation between the final-state medium effects, such as quenching, and the geometry of the hard-scattering processes, such as the path length. For this purpose, collisions of different species should be taken at the same $\sqrt{s_{\mathrm{NN}}}$, with similar pileup and detector conditions. Model studies are forthcoming to put this argument on a more quantitative ground.

3.5 Impact on future experiments: EIC and CBM FAIR

Collisions of isobars may provide valuable input to the physics of the planned EIC. One important goal of the EIC program is to understand the partonic structure of nuclei at very high energy [89, 90]. At small longitudinal momentum fraction, x, the density of gluons may saturate and form the so-called color glass condensate (CGC). EIC will probe gluon saturation using a range of scattering processes in electron-nucleus collisions. In heavy-ion collisions, the modification of parton distributions in nuclei (nPDF) impacts the initial conditions of the QGP, which in turn are imaged via the isobar ratios of bulk and high-p_{T} observables. In this way, one can gain access to the transverse spatial distribution of partons. Exploiting isobar ratios as a function of rapidity,

[1] Although the 20% difference in the mass number between ^{238}U and ^{197}Au seems not too big, the very large deformation of ^{238}U makes it non-trivial to precisely constrain the properties of ^{197}Au (see Ref. [32] for an attempt).

and in particular as a function of $\sqrt{s_{\rm NN}}$, may provide a unique probe of x-dependence of nPDF and gluon saturation. Collisions of the same isobar pair, for example, Ru+Ru and Zr+Zr, at different energies could be realized at CBM FAIR [91] at $\sqrt{s_{\rm NN}} \leq 4.9$ GeV, BNL RHIC at $\sqrt{s_{\rm NN}} = 200$ GeV, and the CERN LHC at $\sqrt{s_{\rm NN}} > 5$ TeV. Any differences between RHIC and LHC in the isobar ratios for soft and hard probes could be used to infer the energy dependence of initial conditions and in turn that of the partonic structure within nuclei. This study will complement the EIC program by providing additional information on the spatial structure of dense gluonic matter. In turn, this information will provide valuable input for the CBM experiment at FAIR in the study of the QCD phase diagram at low temperature and high baryon density [91], in particular, to inform theoretical models such as SMASH [92], AMPT [93], and hydrodynamics [94–98] that aim to describe the dynamical and transport properties of nuclear matter in such conditions.

4 Brief summary of developments since 2022

Since 2022, research devoted to the connection between low-energy nuclear structure and high-energy nuclear collisions has exploded, to the point that it is not possible to cover all the numerous important contributions in this section.

One notable development is the progress made in extracting quantitative information about the structure of nuclei from collider data. Using the Bayesian analysis framework, a recent study demonstrated the possibility of determining the skin of ^{208}Pb from LHC data [99], yielding values that align well with low-energy determinations [72, 100]. Additionally, quantitative insights into nuclear deformations were obtained through comparative measurements of ^{238}U+^{238}U and ^{197}Au+^{197}Au collisions conducted by the STAR Collaboration [101]. When combined with high-precision hydrodynamic calculations and the relatively well-understood, modest quadrupole deformation of ^{197}Au [102, 103], these measurements enabled the quantitative extraction of the intrinsic surface deformation parameters, $\beta_{2\rm U}$ and $\gamma_{\rm U}$, of the ^{238}U nucleus. The results for $\beta_{2\rm U}$ align with low-energy nuclear physics results, while the nonzero value of $\gamma_{\rm U}$ provides evidence for a shape that breaks axial symmetry, shedding light on an aspect of this nucleus that is poorly known in low-energy approaches.

These studies, among others, suggest a wide range of applications for the high-energy nuclear structure imaging method. Potential applications include: systematically determining structural properties of both even- and odd-mass ground states; probing higher-order deformations such as octupole and hexadecapole shapes [103, 104]; discerning the "softness" of the nuclear deformation including the imprint of shape fluctuations or shape coexistence [105], which could reveal nuclear shape phase transitions [106]; and utilizing isobar collisions to aid in the search for neutrinoless double beta decay through complementary tests of theory predictions for nuclear matrix elements [107, 108]. Additionally, progress has been made in formalizing the connection between low-energy theory and high-energy observables based on correlation techniques [109]. The ALICE Collaboration has also performed a measurement of many correlation observables to reveal deformation effects in ^{129}Xe+^{129}Xe collisions [110], although this was limited by event statistics.

Extending these investigations to smaller systems, the influence of nuclear structure on collision observables has also been explored. This is motivated by the availability of high-energy ^{16}O+^{16}O collisions at RHIC [111], which will also be collected at the LHC in summer 2025. As of October 2024, numerous papers have appeared on nuclear clustering effects in high-energy collisions (e.g., [112–114] for recent works). Comparative studies involving light nuclei, such as ^{16}O+^{16}O versus ^{20}Ne+^{20}Ne collisions [115, 116], and ^{16}O+Pb versus ^{20}Ne+Pb collisions [117], predict significant differences beyond model uncertainties. These differences reflect the pronounced structural variations between ^{16}O and ^{20}Ne, including potential alpha clustering effects. Interestingly, high-energy electron-isobar collisions offer another avenue to explore spatial distributions and correlations of nucleons in the ground states, albeit involving different types of observables compared to nucleus–nucleus collisions [109, 118–120].

Furthermore, progress has been made in utilizing nuclear structure to constrain the initial conditions of heavy-ion collisions. Isobar collisions provide a unique opportunity to study the energy dependence and formation mechanisms of these initial conditions [121, 122]. Determining the longitudinal structure of QGP has been particularly challenging due to short-range non-flow effects that contaminate direct measurements; these effects arise from sources like resonance decays and jet fragmentation, which are unrelated to the collective flow. Previous efforts have relied on observables, such as the r_n correlators [123, 124], that do not have a straightforward connection with the longitudinal structure of the initial conditions. Isobar collisions offer a promising solution by allowing us to vary the initial conditions while keeping non-flow effects constant. Due to that, any differences in the longitudinal dependence of observables between isobaric systems can be attributed to changes in their initial conditions. Recent model studies [125, 126] demonstrated that this approach enables the complete subtraction of non-flow influences, effectively isolating the longitudinal structure of the harmonic flow across the entire rapidity range.

5 Summary

A major goal of the hot QCD program, the extraction of the properties of the quark gluon plasma (QGP), is currently limited by our incomplete understanding of the QGP's *initial condition*, particularly how it forms from colliding nuclei. Our proposal is to use collisions of carefully selected species to precisely assess how variations in nuclear structure affect the initial condition. Combining this approach with detailed measurements of particle correlations in the final state of heavy-ion collisions offers a new method to probe the geometries and spatial correlations of nucleons in atomic nuclei. This will enable us to test utilize predictions from state-of-the-art *ab initio* nuclear structure theories in a novel setup. We encourage the U.S. nuclear physics community to seize this interdisciplinary opportunity by pursuing collisions of strategically chosen species at high-energy colliders.

- *Impact on the hot QCD program* Our ability to determine key properties of the QGP from experimental data is limited by our incomplete understanding of its initial conditions immediately after a heavy-ion collision. Colliding nuclear species with significant differences in structural properties provides a new approach to investigate these initial conditions. Specifically, collisions of nuclei that are similar in mass—such as isobars—but different in structure allow us to measure relative changes in observables that are sensitive solely to the QGP initial conditions. These variations stem from "known" structural differences between the species and help us examine precisely how the QGP is formed from the colliding ions. Therefore, future experiments involving isobar collisions with well-known geometries will help reduce uncertainties in determining QGP properties from data.
- *Impact on the nuclear structure program* Explaining the emergence of nuclei from fundamental theory is a major goal of the nuclear structure program, which can benefit from its synergy with the hot QCD program based on high-energy heavy-ion collisions. Due to the short timescales of the interaction processes and the *deterministic* nature of the subsequent hydrodynamic evolution from the initial to the final state, measurements of particle angular correlations in the final states of high-energy collisions are sensitive to many-body correlations of nucleons, such as nuclear deformations, in the colliding nuclei's ground states. High-energy colliders thus provide a novel tool to unravel strongly correlated nuclear systems and test *ab initio* theories of nuclear structure rooted in QCD.
- *Importance of future collider runs* Collisions of different nuclear species will allow us to utilize and test the predictions of cutting-edge *ab initio* nuclear structure methods while simultaneously reducing the uncertainty in the QGP properties derived from data. It is timely to undertake such interdisciplinary studies in upcoming collider runs. These efforts should focus primarily on the CERN LHC in Run4 and Run5 beyond 2025, but also take advantage of opportunities at the BNL RHIC before it gives way to the electron-ion collider (EIC). A better understanding of the role of nuclear structure in high-energy collisions will enhance hydrodynamic or transport model simulations of collisions at RHIC's BES-II, and at the future CBM experiment at FAIR, where the connection between initial conditions and final states is more involved. Additionally, ensuring the robustness of the low-energy inputs will be valuable for studying the modification of parton distributions within nuclei, as planned at the future EIC.

Acknowledgements We thank the participants of the EMMI Rapid Reaction Task Force *"Nuclear physics confronts relativistic collisions of isobars"* (https://indico.gsi.de/event/14430/) for valuable input. This work is supported by U. S. Department of Energy, Office of Science, Office of Nuclear Physics, under Award or Contract No. DE-SC002418 (JDB), DE-SC0024602 (SH, JJ, CZ), DE-SC0004286 (UH), DE-FG02-10ER41666 (CL, WL), DE-SC0013365, DE-SC0024586 and DE-SC0023175 (DL), DE-SC0011088 (YL), DE-AC02-05CH11231 (MP), DE-FG02-89ER40531 (AT), DE-SC0012704 (BS), DE-SC0021969 and DE-SC0024232 (CS), DE-SC0023861 (JN), DE-FG02-07ER41521 (ZX); by National Science Foundation under grant number OAC-2103680 (JN); by European Union (ERC, Initial Conditions), VILLUM FONDEN with grant no. 00025462, and Danmarks Frie Forskningsfond (YZ); and by FAPESP projects 2017/05685-2, 2018/24720-6, and 2021/08465-9, project INCT-FNA Proc.~No.~464898/2014-5, and CAPES - Finance Code 001 (ML).

Funding Open access funding provided by CERN (European Organization for Nuclear Research).

References

1. A. Bohr, B.R. Mottelson (Eds.), Nuclear structure, Vol. I, (World Scientific, 1998). https://doi.org/10.1142/3530
2. D.A. Teaney, Viscous hydrodynamics and the Quark gluon plasma, (2010), pp. 207–266. arXiv:0905.2433, https://doi.org/10.1142/9789814293297_0004

3. W. Busza, K. Rajagopal, W. van der Schee, Heavy ion collisions: the big picture, and the big questions. Ann. Rev. Nucl. Part. Sci. **68**, 339–376 (2018). https://doi.org/10.1146/annurev-nucl-101917-020852. arXiv:1802.04801
4. M. Abdallah et al., Search for the chiral magnetic effect with isobar collisions at $\sqrt{s_{\rm NN}}$=200 GeV by the STAR Collaboration at the BNL Relativistic Heavy Ion Collider. Phys. Rev. C **105**, 014901 (2022). https://doi.org/10.1103/PhysRevC.105.014901. arXiv:2109.00131
5. M.L. Miller, K. Reygers, S.J. Sanders et al., Glauber modeling in high energy nuclear collisions. Ann. Rev. Nucl. Part. Sci. **57**, 205–243 (2007). https://doi.org/10.1146/annurev.nucl.57.090506.12320. arXiv:nucl-ex/0701025
6. Q.Y. Shou, Y.G. Ma, P. Sorensen et al., Parameterization of deformed nuclei for Glauber modeling in relativistic heavy ion collisions. Phys. Lett. B **749**, 215–220 (2015). https://doi.org/10.1016/j.physletb.2015.07.078. arXiv:1409.8375
7. G. Giacalone, A matter of shape: seeing the deformation of atomic nuclei at high-energy colliders. Ph.D. thesis, U. Paris-Saclay (2020). arXiv:2101.00168
8. J. Adam et al., Centrality dependence of the pseudorapidity density distribution for charged particles in Pb-Pb collisions at $\sqrt{s_{\rm NN}}$ = 5.02 TeV. Phys. Lett. B **772**, 567–577 (2017). https://doi.org/10.1016/j.physletb.2017.07.017. arXiv:1612.08966
9. M. Holten, L. Bayha, K. Subramanian et al., Observation of Pauli crystals. Phys. Rev. Lett. **126**, 020401 (2021). https://doi.org/10.1103/PhysRevLett.126.020401. arXiv:2005.03929
10. M. Holten, L. Bayha, K. Subramanian et al., Observation of Cooper pairs in a mesoscopic two-dimensional Fermi gas. Nature **606**, 287–291 (2022). https://doi.org/10.1038/s41586-022-04678-1. arXiv:2109.11511
11. J.E. Bernhard, J.S. Moreland, S.A. Bass et al., Applying Bayesian parameter estimation to relativistic heavy-ion collisions: simultaneous characterization of the initial state and quark-gluon plasma medium. Phys. Rev. C **94**, 024907 (2016). https://doi.org/10.1103/PhysRevC.94.024907. arXiv:1605.03954
12. D. Everett et al., Multisystem Bayesian constraints on the transport coefficients of QCD matter. Phys. Rev. C **103**, 054904 (2021). https://doi.org/10.1103/PhysRevC.103.054904. arXiv:2011.01430
13. G. Nijs, W. van der Schee, U. Gürsoy et al., Transverse momentum differential global analysis of heavy-ion collisions. Phys. Rev. Lett. **126**, 202301 (2021). https://doi.org/10.1103/PhysRevLett.126.202301. arXiv:2010.15130
14. M. Xie, W. Ke, H. Zhang et al., Information field based global Bayesian inference of the jet transport coefficient. arXiv:2206.01340
15. R. Ehlers et al., Bayesian analysis of QGP jet transport using multi-scale modeling applied to inclusive hadron and reconstructed jet data. in 29th International Conference on Ultra-relativistic Nucleus-Nucleus Collisions, 2022. arXiv:2208.07950
16. G. Giacalone, J. Jia, V. Somà, Accessing the shape of atomic nuclei with relativistic collisions of isobars. Phys. Rev. C **104**, L041903 (2021). https://doi.org/10.1103/PhysRevC.104.L041903. arXiv:2102.08158
17. H. Hergert, A guided tour of *abinitio* nuclear many-body theory. Front. in Phys. **8**, 379 (2020). https://doi.org/10.3389/fphy.2020.00379. arXiv:2008.05061
18. J.Y. Ollitrault, Anisotropy as a signature of transverse collective flow. Phys. Rev. D **46**, 229–245 (1992). https://doi.org/10.1103/PhysRevD.46.229
19. B. Alver, G. Roland, Collision geometry fluctuations and triangular flow in heavy-ion collisions. Phys. Rev. C **81**, 054905 (2010). [Erratum: Phys.Rev.C 82, 039903 (2010)]. arXiv:1003.0194, https://doi.org/10.1103/PhysRevC.82.039903
20. D. Teaney, L. Yan, Triangularity and dipole asymmetry in heavy ion collisions. Phys. Rev. C **83**, 064904 (2011). https://doi.org/10.1103/PhysRevC.83.064904. arXiv:1010.1876
21. P. Bozek, W. Broniowski, Transverse-momentum fluctuations in relativistic heavy-ion collisions from event-by-event viscous hydrodynamics. Phys. Rev. C **85**, 044910 (2012). https://doi.org/10.1103/PhysRevC.85.044910. arXiv:1203.1810
22. Haojie Xu talk, Chunjian Zhang poster, (STAR Collabration),Constraints on neutron skin thickness and nuclear deformations using relativistic heavy-ion collisions from STAR, https://indico.cern.ch/event/895086/contributions/4724887/,https://indico.cern.ch/event/895086/contributions/4749420/. (2022)
23. G. Nijs, W. van der Schee, Hadronic nucleus-nucleus cross section and the nucleon size. Phys. Rev. Lett. **129**, 232301 (2022). https://doi.org/10.1103/PhysRevLett.129.232301. arXiv:2206.13522
24. J. Jia, C. Zhang, Scaling approach to nuclear structure in high-energy heavy-ion collisions. Phys. Rev. C **107**, L021901 (2023). https://doi.org/10.1103/PhysRevC.107.L021901. arXiv:2111.15559
25. G. Nijs, W. van der Schee, Inferring nuclear structure from heavy isobar collisions using Trajectum. Sci. Post. Phys. **15**, 041 (2023). https://doi.org/10.21468/SciPostPhys.15.2.041. arXiv:2112.13771
26. S.H. Lim, J. Carlson, C. Loizides et al., Exploring new small system geometries in heavy ion collisions. Phys. Rev. C **99**, 044904 (2019). https://doi.org/10.1103/PhysRevC.99.044904. arXiv:1812.08096
27. M. Rybczyński, W. Broniowski, Glauber Monte Carlo predictions for ultrarelativistic collisions with ^{16}O. Phys. Rev. C **100**, 064912 (2019). https://doi.org/10.1103/PhysRevC.100.064912. arXiv:1910.09489
28. N. Summerfield, B.N. Lu, C. Plumberg et al., ^{16}O^{16}O collisions at energies available at the BNL Relativistic Heavy Ion Collider and at the CERN Large Hadron Collider comparing α clustering versus substructure. Phys. Rev. C **104**, L041901 (2021). https://doi.org/10.1103/PhysRevC.104.L041901. arXiv:2103.03345
29. G. Nijs, W. van der Schee, Predictions and postdictions for relativistic lead and oxygen collisions with the computational simulation code Trajectum. Phys. Rev. C **106**, 044903 (2022). https://doi.org/10.1103/PhysRevC.106.044903. arXiv:2110.13153
30. R.J. Furnstahl, H.W. Hammer, A. Schwenk, Nuclear structure at the crossroads. Few Body Syst. **62**, 72 (2021). https://doi.org/10.1007/s00601-021-01658-5. arXiv:2107.00413
31. G. Giacalone, Elliptic flow fluctuations in central collisions of spherical and deformed nuclei. Phys. Rev. C **99**, 024910 (2019). https://doi.org/10.1103/PhysRevC.99.024910. arXiv:1811.03959
32. G. Giacalone, J. Jia, C. Zhang, Impact of nuclear deformation on relativistic heavy-ion collisions: Assessing consistency in nuclear physics across energy scales. Phys. Rev. Lett. **127**, 242301 (2021). https://doi.org/10.1103/PhysRevLett.127.242301. arXiv:2105.01638
33. J. Jia, Shape of atomic nuclei in heavy ion collisions. Phys. Rev. C **105**, 014905 (2022). https://doi.org/10.1103/PhysRevC.105.014905. arXiv:2106.08768
34. G. Giacalone, J. Noronha-Hostler, M. Luzum et al., Hydrodynamic predictions for 5.44 TeV Xe+Xe collisions. Phys. Rev. C **97**, 034904 (2018). https://doi.org/10.1103/PhysRevC.97.034904. arXiv:1711.08499
35. S. Acharya et al., Anisotropic flow in Xe-Xe collisions at $\sqrt{s_{\rm NN}}$ = **5.44** TeV. Phys. Lett. B **784**, 82–95 (2018). https://doi.org/10.1016/j.physletb.2018.06.059. arXiv:1805.01832

36. B. Schenke, C. Shen, P. Tribedy, Running the gamut of high energy nuclear collisions. Phys. Rev. C **102**, 044905 (2020). https://doi.org/10.1103/PhysRevC.102.044905. arXiv:2005.14682
37. G. Giacalone, Observing the deformation of nuclei with relativistic nuclear collisions. Phys. Rev. Lett. **124**, 202301 (2020). https://doi.org/10.1103/PhysRevLett.124.202301. arXiv:1910.04673
38. P. Bozek, Transverse-momentum-flow correlations in relativistic heavy-ion collisions. Phys. Rev. C **93**, 044908 (2016). https://doi.org/10.1103/PhysRevC.93.044908. arXiv:1601.04513
39. J. Jia, Probing triaxial deformation of atomic nuclei in high-energy heavy ion collisions. Phys. Rev. C **105**, 044905 (2022). https://doi.org/10.1103/PhysRevC.105.044905. arXiv:2109.00604
40. J. Jia, Nuclear deformation effects via Au+Au and U+U collisions from STAR. Contribution to the VI$^{\text{th}}$ International Conference on the Initial Stages of High-Energy Nuclear Collisions, January 2021, https://indico.cern.ch/event/854124/contributions/4135480/ (2021)
41. G. Giacalone, Constraining the quadrupole deformation of atomic nuclei with relativistic nuclear collisions. Phys. Rev. C **102**, 024901 (2020). https://doi.org/10.1103/PhysRevC.102.024901. arXiv:2004.14463
42. L. Vietze, P. Klos, J. Menéndez et al., Nuclear structure aspects of spin-independent WIMP scattering off xenon. Phys. Rev. D **91**, 043520 (2015). https://doi.org/10.1103/PhysRevD.91.043520. arXiv:1412.6091
43. B. Bally, M. Bender, G. Giacalone et al., Evidence of the triaxial structure of ^{129}Xe at the Large Hadron Collider. Phys. Rev. Lett. **128**, 082301 (2022). https://doi.org/10.1103/PhysRevLett.128.082301. arXiv:2108.09578
44. B. Bally, G. Giacalone, M. Bender, Structure of ^{128,129,130}Xe through multi-reference energy density functional calculations. Eur. Phys. J. A **58**, 187 (2022). https://doi.org/10.1140/epja/s10050-022-00833-4. arXiv:2207.13576
45. G. Aad et al., Correlations between flow and transverse momentum in Xe+Xe and Pb+Pb collisions at the LHC with the ATLAS detector: A probe of the heavy-ion initial state and nuclear deformation. Phys. Rev. C **107**, 054910 (2023). https://doi.org/10.1103/PhysRevC.107.054910. arXiv:2205.00039
46. P.A. Butler, W. Nazarewicz, Intrinsic reflection asymmetry in atomic nuclei. Rev. Mod. Phys. **68**, 349–421 (1996). https://doi.org/10.1103/RevModPhys.68.349
47. L.M. Robledo, G.F. Bertsch, Global systematics of octupole excitations in even-even nuclei. Phys. Rev. C **84**, 054302 (2011). https://doi.org/10.1103/PhysRevC.84.054302. arXiv:1107.3581
48. Y. Cao, S.E. Agbemava, A.V. Afanasjev et al., Landscape of pear-shaped even-even nuclei. Phys. Rev. C **102**, 024311 (2020). https://doi.org/10.1103/PhysRevC.102.024311. arXiv:2004.01319
49. L.M. Robledo, G.F. Bertsch, Ground state octupole correlation energy with effective forces. J. Phys. G **42**, 055109 (2015). https://doi.org/10.1088/0954-3899/42/5/055109. arXiv:1408.6941
50. C. Zhang, J. Jia, Evidence of quadrupole and octupole deformations in ^{96}Zr+^{96}Zr and ^{96}Ru+^{96}Ru collisions at ultrarelativistic energies. Phys. Rev. Lett. **128**, 022301 (2022). https://doi.org/10.1103/PhysRevLett.128.022301. arXiv:2109.01631
51. Y.T. Rong, X.Y. Wu, B.N. Lu et al., Anatomy of octupole correlations in ^{96}Zr with a symmetry-restored multidimensionally-constrained covariant density functional theory. Phys. Lett. B **840**, 137896 (2023). https://doi.org/10.1016/j.physletb.2023.137896. arXiv:2201.02114
52. H. Li, H.J. Xu, Y. Zhou et al., Probing the neutron skin with ultrarelativistic isobaric collisions. Phys. Rev. Lett **125**, 222301 (2020). https://doi.org/10.1103/PhysRevLett.125.222301. arXiv:1910.06170
53. Hj. Xu, W. Zhao, H. Li et al., Probing nuclear structure with mean transverse momentum in relativistic isobar collisions. Phys. Rev. C **108**, L011902 (2023). https://doi.org/10.1103/PhysRevC.108.L011902. arXiv:2111.14812
54. C. Zhang, S. Bhatta, J. Jia, Ratios of collective flow observables in high-energy isobar collisions are insensitive to final state interactions. Phys. Rev. C **106**, L031901 (2022). https://doi.org/10.1103/PhysRevC.106.L031901. arXiv:2206.01943
55. Z.W. Lin, C.M. Ko, B.A. Li et al., A Multi-phase transport model for relativistic heavy ion collisions. Phys. Rev. C **72**, 064901 (2005). https://doi.org/10.1103/PhysRevC.72.064901. arXiv:nucl-th/0411110
56. H. Li, H..j Xu, J. Zhao et al., Multiphase transport model predictions of isobaric collisions with nuclear structure from density functional theory. Phys. Rev. C **98**, 054907 (2018). https://doi.org/10.1103/PhysRevC.98.054907. arXiv:1808.06711
57. Hj. Xu, H. Li, X. Wang et al., Determine the neutron skin type by relativistic isobaric collisions. Phys. Lett. B **819**, 136453 (2021). https://doi.org/10.1016/j.physletb.2021.136453. arXiv:2103.05595
58. S.A. Voloshin, A.M. Poskanzer, A. Tang et al., Elliptic flow in the Gaussian model of eccentricity fluctuations. Phys. Lett. B **659**, 537–541 (2008). https://doi.org/10.1016/j.physletb.2007.11.043. arXiv:0708.0800
59. J. Jia, G. Giacalone, C. Zhang, Separating the impact of nuclear skin and nuclear deformation in high-energy isobar collisions. Phys. Rev. Lett. **131**, 022301 (2023). https://doi.org/10.1103/PhysRevLett.131.022301. arXiv:2206.10449
60. X. Viñas, M. Centelles, X. Roca-Maza et al., Density dependence of the symmetry energy from neutron skin thickness in finite nuclei. Eur. Phys. J. A **50**, 27 (2014). https://doi.org/10.1140/epja/i2014-14027-8. arXiv:1308.1008
61. J.M. Lattimer, M. Prakash, Neutron star observations: prognosis for equation of state constraints. Phys. Rept. **442**, 109–165 (2007). https://doi.org/10.1016/j.physrep.2007.02.003. arXiv:astro-ph/0612440
62. B.A. Li, L.W. Chen, C.M. Ko, Recent progress and new challenges in isospin physics with heavy-ion reactions. Phys. Rept. **464**, 113–281 (2008). https://doi.org/10.1016/j.physrep.2008.04.005. arXiv:0804.3580
63. H. Horiuchi, K. Ikeda, A molecule-like structure in atomic nuclei of $^{16}O^{*}$ and ^{20}Ne. Prog. Theor. Phys. **40**, 277–287 (1968). https://doi.org/10.1143/PTP.40.277
64. J.P. Ebran, E. Khan, T. Nikšić et al., How atomic nuclei cluster. Nature **487**, 341–344 (2012). https://doi.org/10.1038/nature11246. arXiv:2109.11511
65. E.F. Zhou, J.M. Yao, Z.P. Li et al., Anatomy of molecular structures in ^{20}Ne. Phys. Lett. B **753**, 227–231 (2016). https://doi.org/10.1016/j.physletb.2015.12.028. arXiv:1510.05232
66. M. Frosini, T. Duguet, J.P. Ebran et al., Multi-reference many-body perturbation theory for nuclei: II. Ab initio study of neon isotopes via PGCM and IM-NCSM calculations. Eur. Phys. J. A **58**, 63 (2022). https://doi.org/10.1140/epja/s10050-022-00693-y. arXiv:2111.00797
67. R. Aaij et al., Centrality determination in heavy-ion collisions with the LHCb detector. JINST **17**, P05009 (2022). https://doi.org/10.1088/1748-0221/17/05/P05009. arXiv:2111.01607
68. W. Broniowski, E. Ruiz Arriola, Signatures of α clustering in light nuclei from relativistic nuclear collisions. Phys. Rev. Lett **112**, 112501 (2014). https://doi.org/10.1103/PhysRevLett.112.112501. arXiv:1312.0289
69. M. Rybczyński, M. Piotrowska, W. Broniowski, Signatures of α clustering in ultrarelativistic collisions with light nuclei. Phys.

Rev. C **97**, 034912 (2018). https://doi.org/10.1103/PhysRevC.97.034912. arXiv:1711.00438
70. C. Aidala et al., Creation of quark-gluon plasma droplets with three distinct geometries. Nat. Phys. **15**, 214–220 (2019). https://doi.org/10.1038/s41567-018-0360-0. arXiv:1805.02973
71. LHCb Collaboration, LHCb SMOG Upgrade. Tech. rep., CERN, Geneva (2019). https://doi.org/10.17181/CERN.SAQC.EOWH
72. D. Adhikari et al., Accurate determination of the neutron skin thickness of ^{208}Pb through parity-violation in electron scattering. Phys. Rev. Lett. **126**, 172502 (2021). https://doi.org/10.1103/PhysRevLett.126.172502. arXiv:2102.10767
73. D. Adhikari et al., Precision determination of the neutral weak form factor of ^{48}Ca. Phys. Rev. Lett. **129**, 042501 (2022). https://doi.org/10.1103/PhysRevLett.129.042501. arXiv:2205.11593
74. F.J. Fattoyev, J. Piekarewicz, C.J. Horowitz, Neutron skins and neutron stars in the multimessenger era. Phys. Rev. Lett. **120**, 172702 (2018). https://doi.org/10.1103/PhysRevLett.120.172702. arXiv:1711.06615
75. B.T. Reed, F.J. Fattoyev, C.J. Horowitz et al., Implications of PREX-2 on the equation of state of neutron-rich matter. Phys. Rev. Lett. **126**, 172503 (2021). https://doi.org/10.1103/PhysRevLett.126.172503. arXiv:2101.03193
76. C.W.P. Palmer, P.E.G. Baird, S.A. Blundell et al., Laser spectroscopy of calcium isotopes. J. Phys. B: Atom. Mol. Phys. **17**, 2197 (1984). https://doi.org/10.1088/0022-3700/17/11/014
77. R.F. Garcia Ruiz et al., Unexpectedly large charge radii of neutron-rich calcium isotopes. Nat. Phys. **12**, 594 (2016). https://doi.org/10.1038/nphys3645. arXiv:1602.07906
78. M. Abdallah et al., Tomography of ultrarelativistic nuclei with polarized photon-gluon collisions. Sci. Adv. **9**, eabq3903 (2023). https://doi.org/10.1126/sciadv.abq3903. arXiv:2204.01625
79. H. Paukkunen, Neutron skin and centrality classification in high-energy heavy-ion collisions at the LHC. Phys. Lett. B **745**, 73–78 (2015). https://doi.org/10.1016/j.physletb.2015.04.037. arXiv:1503.02448
80. G. Aad et al., Measurement of $W^{\pm}$ boson production in Pb+Pb collisions at $\sqrt{s_{\rm NN}} = 5.02$ TeV with the ATLAS detector. Eur. Phys. J. C **79**, 935 (2019). https://doi.org/10.1140/epjc/s10052-019-7439-3. arXiv:1907.10414
81. G. Aad et al., Z boson production in Pb+Pb collisions at $\sqrt{s_{\rm NN}}$= 5.02 TeV measured by the ATLAS experiment. Phys. Lett. B **802**, 135262 (2020). https://doi.org/10.1016/j.physletb.2020.135262. arXiv:1910.13396
82. Z. Citron et al., Report from Working Group 5: Future physics opportunities for high-density QCD at the LHC with heavy-ion and proton beams. CERN Yellow Rep. Monogr. **7**, 1159–1410 (2019). https://doi.org/10.23731/CYRM-2019-007.1159. arXiv:1812.06772
83. R. Bruce, M.A. Jebramcik, J.M. Jowett et al., Performance and luminosity models for heavy-ion operation at the CERN Large Hadron Collider. Eur. Phys. J. Plus **136**, 745 (2021). https://doi.org/10.1140/epjp/s13360-021-01685-5. arXiv:2107.09560
84. F. Gelis, E. Iancu, J. Jalilian-Marian et al., The Color Glass Condensate. Ann. Rev. Nucl. Part. Sci. **60**, 463–489 (2010). https://doi.org/10.1146/annurev.nucl.010909.083629. arXiv:1002.0333
85. F. Gelis, *Quantum Field Theory* (Cambridge University Press, Cambridge, 2019)
86. J.S. Moreland, J.E. Bernhard, S.A. Bass, Alternative ansatz to wounded nucleon and binary collision scaling in high-energy nuclear collisions. Phys. Rev. C **92**, 011901 (2015). https://doi.org/10.1103/PhysRevC.92.011901. arXiv:1412.4708
87. G. Giacalone, There and sharp again: the circle journey of nucleons and energy deposition. Acta Phys. Polonica B Proc. Suppl. **16**, 1–10 (2022). arXiv:2208.06839
88. R. Katz, C.A.G. Prado, J. Noronha-Hostler et al., System-size scan of D meson R_{AA} and v_n using PbPb, XeXe, ArAr, and OO collisions at energies available at the CERN Large Hadron Collider. Phys. Rev. C **102**, 041901 (2020). https://doi.org/10.1103/PhysRevC.102.041901. arXiv:1907.03308
89. A. Accardi et al., Electron ion collider: the next QCD frontier: understanding the glue that binds us all. Eur. Phys. J. A **52**, 268 (2016). https://doi.org/10.1140/epja/i2016-16268-9. arXiv:1212.1701
90. R. Abdul Khalek et al., Science requirements and detector concepts for the electron-ion collider: EIC yellow report. Nucl. Phys. A **1026**, 122447 (2022). https://doi.org/10.1016/j.nuclphysa.2022.122447. arXiv:2103.05419
91. D. Almaalol et al., QCD Phase Structure and Interactions at High Baryon Density: Completion of BES Physics Program with CBM at FAIR. arXiv:2209.05009
92. J. Weil et al., Particle production and equilibrium properties within a new hadron transport approach for heavy-ion collisions. Phys. Rev. C **94**, 054905 (2016). https://doi.org/10.1103/PhysRevC.94.054905. arXiv:1606.06642
93. Z.W. Lin, L. Zheng, Further developments of a multi-phase transport model for relativistic nuclear collisions. Nucl. Sci. Tech. **32**, 113 (2021). https://doi.org/10.1007/s41365-021-00944-5. arXiv:2110.02989
94. C. Shen, L. Yan, Recent development of hydrodynamic modeling in heavy-ion collisions. Nucl. Sci. Tech. **31**, 122 (2020). https://doi.org/10.1007/s41365-020-00829-z. arXiv:2010.12377
95. C. Shen, B. Schenke, Dynamical initial state model for relativistic heavy-ion collisions. Phys. Rev. C **97**, 024907 (2018). https://doi.org/10.1103/PhysRevC.97.024907. arXiv:1710.00881
96. C. Spieles, M. Bleicher, Effects of the QCD phase transition on hadronic observables in relativistic hydrodynamic simulations of heavy-ion reactions in the FAIR/NICA energy regime. Eur. Phys. J. ST **229**, 3537–3550 (2020). https://doi.org/10.1140/epjst/e2020-000102-4. arXiv:2006.01220
97. M. Bluhm et al., Dynamics of critical fluctuations: theory - phenomenology - heavy-ion collisions. Nucl. Phys. A **1003**, 122016 (2020). https://doi.org/10.1016/j.nuclphysa.2020.122016. arXiv:2001.08831
98. X. An et al., The BEST framework for the search for the QCD critical point and the chiral magnetic effect. Nucl. Phys. A **1017**, 122343 (2022). https://doi.org/10.1016/j.nuclphysa.2021.122343. arXiv:2108.13867
99. G. Giacalone, G. Nijs, W. van der Schee, Determination of the neutron skin of Pb208 from ultrarelativistic nuclear collisions. Phys. Rev. Lett. **131**, 202302 (2023). https://doi.org/10.1103/PhysRevLett.131.202302. arXiv:2305.00015
100. B. Hu et al., Ab initio predictions link the neutron skin of ^{208}Pb to nuclear forces. Nat. Phys. **18**, 1196–1200 (2022). https://doi.org/10.1038/s41567-023-02324-9. arXiv:2112.01125
101. STAR Collaboration, Imaging shapes of atomic nuclei in high-energy nuclear collisions. Nature **635**, 67–72 (2024). https://doi.org/10.1038/s41586-024-08097-2. arXiv:2401.06625
102. B. Bally, G. Giacalone, M. Bender, The shape of gold. Eur. Phys. J. A **59**, 58 (2023). https://doi.org/10.1140/epja/s10050-023-00955-3. arXiv:2301.02420
103. W. Ryssens, G. Giacalone, B. Schenke et al., Evidence of hexadecapole deformation in Uranium-238 at the relativistic heavy ion collider. Phys. Rev. Lett. **130**, 212302 (2023). https://doi.org/10.1103/PhysRevLett.130.212302
104. Hj. Xu, J. Zhao, F. Wang, Hexadecapole deformation of ^{238}U from relativistic heavy-ion collisions using a nonlinear response coefficient. Phys. Rev. Lett **132**, 262301 (2024). https://doi.org/10.1103/PhysRevLett.132.262301. arXiv:2402.16550
105. A. Dimri, S. Bhatta, J. Jia, Impact of nuclear shape fluctuations in high-energy heavy ion collisions. Eur. Phys. J. A **59**, 45 (2023). https://doi.org/10.1140/epja/s10050-023-00965-1

106. S. Zhao, H.J. Xu, Y. Zhou et al., Exploring the Nuclear Shape Phase Transition in Ultra-Relativistic ^{129}Xe+^{129}Xe Collisions at the LHC. Phys. Rev. Lett. **133**, 192301. https://doi.org/10.1103/PhysRevLett.133.192301 arXiv:2403.07441
107. A. Belley, J. Pitcher, T. Miyagi et al., Correlation of neutrinoless double-beta decay nuclear matrix elements with nucleon-nucleon phase shifts. arXiv:2408.02169
108. X. Zhang, C.C. Wang, C.R. Ding et al., Global sensitivity analysis and uncertainty quantification of nuclear low-lying states and double-beta decay with a covariant energy density functional. arXiv:2408.13209
109. G. Giacalone, Many-body correlations for nuclear physics across scales: from nuclei to quark-gluon plasmas to hadron distributions. Eur. Phys. J. A **59**, 297 (2023). https://doi.org/10.1140/epja/s10050-023-01200-7. arXiv:2305.19843
110. S. Acharya et al., Exploring nuclear structure with multiparticle azimuthal correlations at the LHC. arXiv:2409.04343
111. S. Huang, Measurements of azimuthal anisotropies in ^{16}O+^{16}O and γ+Au collisions from STAR. 2023. arXiv:2312.12167
112. Y. Wang, S. Zhao, B. Cao et al., Exploring the compactness of α clusters in ^{16}O nuclei with relativistic ^{16}O+^{16}O collisions. Phys. Rev. C **109**, L051904 (2024). https://doi.org/10.1103/PhysRevC.109.L051904. arXiv:2401.15723
113. C. Zhang, J. Chen, G. Giacalone et al., *Ab-initio* nucleon-nucleon correlations and their impact on high energy ^{16}O+^{16}O collisions. arXiv:2404.08385
114. S. Prasad, N. Mallick, R. Sahoo et al., Anisotropic flow fluctuation as a possible signature of clustered nuclear geometry in O-O collisions at the Large Hadron Collider. arXiv:2407.15065
115. C. Ding, L.G. Pang, S. Zhang et al., Signals of α clusters in ^{16}O+^{16}O collisions at the LHC from relativistic hydrodynamic simulations. Chin. Phys. C **47**, 024105 (2023). https://doi.org/10.1088/1674-1137/ac9fb8
116. G. Giacalone et al., The unexpected uses of a bowling pin: exploiting ^{20}Ne isotopes for precision characterizations of collectivity in small systems. arXiv:2402.05995
117. G. Giacalone et al., The unexpected uses of a bowling pin: anisotropic flow in fixed-target ^{208}Pb+^{20}Ne collisions as a probe of quark-gluon plasma. arXiv:2405.20210
118. H. Mäntysaari, B. Schenke, C. Shen et al., Multiscale imaging of nuclear deformation at the electron-ion collider. Phys. Rev. Lett. **131**, 062301 (2023). https://doi.org/10.1103/PhysRevLett.131.062301. arXiv:2303.04866
119. S. Lin, J.Y. Hu, H.J. Xu et al., Nuclear deformation effects in photoproduction of ρ mesons in ultraperipheral isobaric collisions. arXiv:2405.16491
120. N. Magdy, M. Hegazy, A. Rafaat et al., A study of nuclear structure of light nuclei at the Electron-Ion Collider. arXiv:2405.07844
121. F. Li, Y.G. Ma, S. Zhang et al., Impact of nuclear structure on the background in the chiral magnetic effect in $^{96}_{44}$Ru + $^{96}_{44}$Ru and $^{96}_{40}$Zr + $^{96}_{40}$Zr collisions at $\sqrt{s_{NN}}$ = 7.7 ~ 200 GeV from a multiphase transport model. Phys. Rev. C **106**, 014906 (2022). arXiv:2201.10994, https://doi.org/10.1103/PhysRevC.106.014906
122. S. Bhatta, C. Zhang, J. Jia, Energy dependence of heavy-ion initial condition in isobar collisions. Phys. Lett. B **858**, 139034 (2024). https://doi.org/10.1016/j.physletb.2024.139034. arXiv:2301.01294
123. V. Khachatryan et al., Evidence for transverse momentum and pseudorapidity dependent event plane fluctuations in PbPb and pPb collisions. Phys. Rev. C **92**, 034911 (2015). https://doi.org/10.1103/PhysRevC.92.034911. arXiv:1503.01692
124. M. Aaboud et al., Measurement of longitudinal flow decorrelations in Pb+Pb collisions at $\sqrt{s_{\rm NN}}$ = 2.76 and 5.02 TeV with the ATLAS detector. Eur. Phys. J. C **78**, 142 (2018). https://doi.org/10.1140/epjc/s10052-018-5605-7. arXiv:1709.02301
125. C. Zhang, S. Huang, J. Jia, Longitudinal structure of quark-gluon plasma unveiled through nuclear deformations. arXiv:2405.08749
126. J. Jia, S. Huang, C. Zhang et al., Sources of longitudinal flow decorrelations in high-energy nuclear collisions. arXiv:2408.15006

Authors and Affiliations

Jiangyong Jia[1,2] · Giuliano Giacalone[3] · Benjamin Bally[4] · James Daniel Brandenburg[5] · Ulrich Heinz[5] · Shengli Huang[1] · Dean Lee[6] · Yen-Jie Lee[7] · Constantin Loizides[8] · Wei Li[8] · Matthew Luzum[9] · Govert Nijs[3] · Jacquelyn Noronha-Hostler[10] · Mateusz Ploskon[11] · Wilke van der Schee[3] · Bjoern Schenke[2] · Chun Shen[12,13] · Vittorio Somà[4] · Anthony Timmins[14] · Zhangbu Xu[2,15] · You Zhou[16]

✉ Jiangyong Jia
jiangyong.jia@stonybrook.edu

✉ Giuliano Giacalone
giulianogiacalone@gmail.com

[1] Stony Brook University, Stony Brook, NY 11794, USA

[2] Brookhaven National Laboratory, Upton, NY 11973, USA

[3] CERN, CH-1211 Geneve 23, Switzerland

[4] IRFU, CEA, Université Paris-Saclay, 91191 Gif-sur-Yvette, France

[5] The Ohio State University, Columbus, OH 43210-1117, USA

[6] Michigan State University, East Lansing, MI 48824, USA

[7] Massachusetts Institute of Technology, Cambridge, MA 02139, USA

[8] Rice University, Houston, TX 77005, USA

[9] Instituto de Física, Universidade de São Paulo, R. do Matão 1371, São Paulo 05508-090, Brazil

[10] University of Illinois at Urbana-Champaign, Champaign, IL 61801, USA

[11] Lawrence Berkeley National Laboratory, Berkeley, CA 94720, USA

[12] Wayne State University, Detroit, MI 48201, USA

[13] RIKEN BNL Research Center, Brookhaven National Laboratory, Upton, NY 11973, USA

[14] University of Houston, Houston, TX 77204, USA

[15] Physics Department, Kent State University, Kent, OH 44242, USA

[16] Niels Bohr Institute, University of Copenhagen, Blegdamsvej 17, 2100 Copenhagen, Denmark